In vitro corrosion and biocompatibility behavior of CoCrMo alloy manufactured by laser powder bed fusion parallel and perpendicular to the build direction

Masoud Atapour [a,b,*], Saber Sanaei [a], Zheng Wei [b], Mohammadali Sheikholeslam [c], Jeffrey D. Henderson [d], Ubong Eduok [b], Yara K. Hosein [e], David W. Holdsworth [f], Yolanda S. Hedberg [b,d,*], Hamid Reza Ghorbani [a]

[a] *Department of Materials Engineering, Isfahan University of Technology, Isfahan 84156-83111, Iran*
[b] *Department of Chemistry, The University of Western Ontario, London, Ontario N6A 5B7, Canada*
[c] *Department of Biomaterials, Tissue Engineering and Nanotechnology, School of Advanced Technologies in Medicine, Isfahan University of Medical Sciences, Isfahan 81746-73461, Iran*
[d] *Surface Science Western, The University of Western Ontario, London, Ontario N6G 0J3, Canada*
[e] *Additive Design in Surgical Solutions Centre, The University of Western Ontario, London, Ontario N6G 4X8, Canada*
[f] *Department of Medical Biophysics, The University of Western Ontario, London, Ontario N6A 5C1, Canada*

ARTICLE INFO

ABSTRACT

Biomedical cobalt-chromium-molybdenum alloys (CoCrMo) are frequently used for orthopedic implant and dental materials exposed to mechanical stressors, such as wear and cyclic load. Due to the high demand for customizable implant shapes, these alloys are increasingly manufactured by additive manufacturing methods such as laser powder bed fusion (LPBF). LPBF results in different microstructures and surface roughness as a function of the building direction. This study investigated the corrosion resistance, bioactivity, biocompatibility, and microstructure of LPBF CoCrMo (low carbon content, heat-treated) in the XY (perpendicular) and XZ (parallel) plane of the building direction for as-printed (as-received) and abraded surfaces. A distinct microstructure and different surface roughness were found for the XY and XZ planes. The as-received XY surface showed the lowest corrosion resistance but was still passive in phosphate-buffered saline (PBS, pH 7.4). As-received surfaces were less corrosion-resistant than abraded surfaces. All specimens exhibited lower corrosion resistance in PBS containing citric acid at pH 7.4 than in PBS and citric acid alone. As-received surfaces showed better hydroxyapatite precipitation and cell viability; however, all surfaces had satisfactory biocompatibility and bioactivity. This study showed that the building direction had a minor effect on the corrosion of LPBF CoCrMo.

1. Introduction

The demand for high-performance orthopedic biomaterials has grown dramatically in the last decades, driven by the rise in the geriatric population, rising bone diseases, and improving living standards [1]. Ceramic and metallic biomaterials exhibit strength, toughness, modulus, and fracture and fatigue resistance [2]. Still, some challenges of orthopedic and dental biomaterials are improving the bio-functionality and reducing the relatively high manufacturing costs [3]. Additive manufacturing (AM) has recently become a key technology to overcome these challenges. Also, due to its greater customizability, speed, and accuracy, additive manufacturing attracted increasing attention for industrial manufacturing of metallic implants [4,5].

Among different metallic biomaterials, cobalt-chromium-molybdenum (CoCrMo) alloys offer unique mechanical properties and low wear and corrosion rates [6]. These implant materials are conventionally produced by casting and forging processes. In recent years, AM technologies, including Laser Powder Bed Fusion (LPBF), have made significant progress in manufacturing hip, knee, and spinal implant applications [7–9]. The fabrication of customized implants by AM technology can address some key challenges, such as the design of implants that are a mismatch between the joint prosthesis and bone,

---

non-physiological load bearing, and unsatisfactory osteointegration [10]. However, components manufactured by LPBF are characterized by non-equilibrium physical, metallurgical and chemical properties. The formation of porosity, high residual stresses and defects are some of the main challenges associated with LPBF CoCrMo [11]. The corrosion behavior is another critical issue since the release of Co and Cr ions and the formation of corrosion products cause adverse health effects [12, 13]. Also, it has been reported that metal ion release associated with wear and corrosion [14,15] plays a vital role in the biocompatibility of CoCrMo alloys [8].

Various investigations focused on the corrosion aspects of CoCrMo alloys fabricated by AM methods. Hedberg et al. [16] investigated the corrosion behavior of LPBF CoCrMo compared with its cast counterpart and reported superior behavior of the LPBF alloy. A study on laser metal-deposited CoCrMo indicated that the formation of fine grains and a low extent of Mo segregation could improve corrosion resistance [17]. Also, the content and distribution of precipitates have been reported to influence the corrosion resistance of LPBF CoCrMoW alloy [18]. In another study on the corrosion of LPBF CoCrMo, it was stated that the plane parallel to the build direction (XZ plane) released more metal ions than those in the XY plane [19].

In addition to the AM microstructure aspects, the surface roughness of the AM metallic specimens is a decisive factor influencing their corrosion properties and biocompatibility [20,21]. This study aimed to investigate the corrosion resistance, bioactivity, biocompatibility, and microstructure of LPBF CoCrMo (low carbon content) in the XY and XZ plane of the building direction for as-printed and abraded surfaces. To simulate a physiological environment, citric acid was added to phosphate-buffered saline (PBS) at pH 7.4. It has previously been shown that citric acid species are strongly metal complexing agents at neutral pH [22,23] and induce similar metal release and corrosion as protein environments [24,25]. For reference, PBS without citric acid and citric acid without a buffer are also included in this study.

2. Materials and methods

2.1. Sample fabrication and characterization

The alloy in this study was fabricated from an inert gas-atomized powder (chemical composition in Table 1) and purchased from Renishaw, UK, with a mean particle size of approximately 15–45 μm. Rectangular alloy specimens (15 mm × 15 mm × 2 mm) were fabricated by the LPBF method using optimized industrial parameters for fully dense specimens and a Renishaw AM400 Selective Laser Melting System (ADEISS, London, Canada). Two types of specimens were fabricated; one placed parallel and the other perpendicular to the building direction, denoted as XZ and XY, respectively. The processing parameters are listed in Table 2 and one layer was rotated 67° to the previous layer. After fabrication, these specimens were heat treated with a particular route as follows: (1) the specimens were gradually heated to 450 °C for 60 min, (2) then kept at this temperature for 45 min, (3) then reheated to 750 °C for 45 min, (4) then kept at this temperature for 60 min, and (5) furnace cooled to room temperature. After the heat treatment, the surfaces were sandblasted using a dental sandblasting mixture (with 63–125 μm zirconia with 28–33 wt.% silica and less than 10 wt.% alumina), ultrasonically cleaned in isopropyl alcohol and deionized water, and dried in a convection oven. This surface finish is denoted 'as-received'. Half of the specimens were further abraded using P1200 SiC paper with deionized water as a lubricant, followed by ultrasonic cleaning in acetone and ethanol (5 min each) and drying using nitrogen gas,

Table 2
LPBF setup and parameters.

Power	Spot size	Scan speed	Layer thickness	Scan spacing
200 W	70 μm	2 m/s	40 μm	70 μm

denoted 'abraded'.

2.2. Microstructure and surface roughness characterization

Before microstructural analyses, all specimens were polished with 0.25 μm diamond paste and then electropolished for 20 s at 4 V using a 1:9 (by volume) solution of HCl and H_2O. Optical microscopy (OM, Nikon EpipHot 300) and scanning electron microscopy (SEM, Philips XL 30) techniques were utilized for characterization. Phase identification was also conducted using X-ray diffraction (XRD, Phillips, Netherlands) equipped with a CuK_α radiation source ($\lambda = 0.154$ nm, 40 kV, 40 mA) scanning from 20 to 80° (2Θ). The roughness value (R_a) of different specimens was determined using a Stylus profilometer (Mitutoyo SJ210). In addition, surface topography mapping and roughness measurements were performed using a ZEISS LSM 800 confocal microscope manufactured by Carl Zeiss Microscopy GmbH. The surface roughness and surface area were calculated using version 7.4.8341 of Mountains ConfoMap software. The calculations were performed by the standard ISO 25178-2:2012.

2.3. X-ray photoelectron spectroscopy (XPS)

XPS can probe the outermost (7–10 nm) surface of the specimens and was used to characterize the surface composition of unexposed as-received XY, as-received XZ, abraded XY and abraded XZ specimens. The XPS analyses were carried out with a Kratos AXIS Supra X-ray photoelectron spectrometer using a monochromatic Al K_α source (15 mA, 15 kV). XPS has detection limits ranging from 0.1 to 0.5 at.% depending on the element. The instrument work function was calibrated to give a binding energy (BE) of 83.96 eV for the Au 4f7/2 line for metallic gold. The spectrometer dispersion was adjusted to give a BE of 932.62 eV for the Cu 2p3/2 line of metallic copper. The Kratos charge neutralizer system was used on all specimens. All specimens were mounted electrically isolated from the instrument sample holder for these analyses. For all measurements, survey scan analyses were carried out with an analysis area of 300 × 700 μm and a pass energy of 160 eV, and high-resolution analyses were carried out with an analysis area of 300 × 700 μm and a pass energy of 20 eV. High-resolution C 1s, O 1s, Si 2p (selected samples), Co 2p, Cr 2p, and Mo 3d were run. All high-resolution spectra were charge-corrected using adventitious carbon (C 1s, 284.8 eV). Peak convolution was conducted according to previously published protocols [26–28].

2.4. Corrosion studies

The corrosion behavior of the printed specimens was assessed using electrochemical impedance spectroscopy (EIS) and potentiodynamic polarization in three solutions of phosphate-buffered saline (PBS, 8.77 g/L NaCl, 1.28 g/L Na_2HPO_4, 1.36 g/L KH_2PO_4, 350 μL/L 50% NaOH, pH 7.2–7.4,), citric acid (CA, 5 g/L citric acid, pH=2.40), and CA + PBS (pH = 7. 40) solutions. The choice of citrate-containing PBS was based on its similarity to many biological environments, including protein environments, due to its complexation capacity [22–25]. Citrate has

Table 1
As per supplier information, chemical composition of CoCrMo (F75) alloy powder.

Element	Cr	Mo	Mn	Si	N	Fe	Ni	C	W	Co
wt.%	28.0	6.10	0.77	0.57	0.22	0.20	0.05	0.02	0.02	Bal.

been used as a simplified model molecule for many physiological solutions [29–32]. PBS without CA and CA without a buffer served as reference solutions.

These evaluations were conducted in a three-electrode system, with a Ag/AgCl (saturated KCl) reference electrode, platinum counter electrode sheet and CoCrMo specimens as working electrodes, all coupled to an AMETEK potentiostat/galvanostat (PARSTAT 2273). Before each test, the specimens were immersed for 45 min, and the open circuit potential (OCP) was measured to reach a steady state condition. EIS tests were conducted at OCP with an alternating current (AC) amplitude of 10 mV$_{rms}$ and a frequency range of 100,000 to 0.01 Hz. The potentiodynamic polarization tests were conducted from −250 to 1500 mV vs. open circuit potential with a scanning rate of 1 mV/s. Selected corrosion parameters (i_{corr}, β_a, β_c and E_{corr}) were obtained based on the Tafel extrapolation method.

2.5. Bioactivity studies

To investigate hydroxyapatite formation on the surface (in the following referred to as "bioactivity") of the printed specimens and the effect of grinding (with P1200 SiC paper), the specimens were immersed in 20 mL simulated body fluid (SBF) and incubated at 37 °C for 7, 14 and 28 days (no shaking) in an incubator (Memmert GmbH, Germany) to prevent being exposed to the light. After immersion, the specimens were removed from the SBF, rinsed with distilled water, and dried in an oven. The surface morphology and composition (information depth of micrometers) were studied using scanning electron microscopy (SEM; SE detector; Philips XI30) and energy dispersive X-ray spectroscopy (EDX). The composition of SBF is depicted in Table 3.

2.6. Cell culture

Osteoblast-like MG63 cells (Pasteur Institute of Iran, Iran) were aseptically cultured in DMEM (Dulbecco's Modified Eagle Medium) supplemented with 10% fetal bovine serum (FBS) and 1% penicillin/streptomycin (Sigma-Aldrich Co; USA) at 37 °C in a humidified 5% CO$_2$ incubator in the dark. The media was exchanged 2–3 times per week, and the cells were sub-cultured at 80% confluency. Rectangular 5 × 5 mm^2 scaffolds were sterilized in 70% ethanol for 1 h, followed by UV irradiation of both sides for 1 h. The sterilized scaffolds were submerged in the cell culture medium overnight, and then the media inside the wells were aspirated, and the cells were seeded on top of the scaffolds. The cells were used at passage 5−7 and seeded at a 5 × 10^3 cell/scaffold density before adding 500 μL of cell culture medium to each well. To enhance the seeding efficiency, the cells were added in a minimal volume of media (i.e., 10 μL). Then 500 μL of culturing media was added after 10 min to enable sufficient adherence of the cells to the scaffold. The scaffolds were kept at 37 °C in a humidified 5% CO$_2$ condition, and the media was changed every second day until the end of the experiment on day 7.

2.7. Cell adhesion and morphological characterization

The morphology of adhered cells on the specimens was visualized by

Table 3
Composition of the simulated body fluid (SBF), with pH 7.4, adjusted with 1 M HCl; adapted from [33].

Reagent	Composition (g/L)
NaCl	8.035
NaHCO$_3$	0.355
KCl	0.225
K$_2$HPO$_4\cdot$3H$_2$O	0.231
MgCl$_2\cdot$6H$_2$O	0.311
CaCl$_2$	0.292
Na$_2$SO$_4$	0.072

SEM. After 7 days, the cells on the specimens were washed with PBS, then fixed with 4% (w/v) PFA (paraformaldehyde) in PBS for 30 min at 37 °C. After three times washing with PBS, the cell-seeded surfaces were dehydrated before SEM imaging by successive immersions in 30%, 50%, 70%, 90%, and 100% ethanol solutions for 30 min at each concentration. They were then submerged in 100% hexamethyldisilazane (Sigma-Aldrich Co; USA) for another 30 min at room temperature and finally imaged by SEM after complete drying in air.

2.8. Cell viability

The relative (to negative control) viability of cells seeded on the specimens was studied by the MTT assay. MTT stands for 3-(4,5-dimethylthiazol-2-yl)−2,5-diphenyltetrazolium bromide (Sigma-Aldrich Co; USA). MTT solution (0.5 mg/ml in DMEM and penicillin/streptomycin without FBS) was prepared fresh and filtered (0.2 μm cellulose membrane Syringe Filter) at each time point (i.e., day 1, 3 & 7). After these time points, the culture medium (DMEM) in the wells was completely replaced with 300 μL MTT solution. The cells were incubated at 37 °C under a 5% CO$_2$ atmosphere for 4 h. Then, the MTT solutions were aspirated, and 300 μL dimethyl sulfoxide (DMSO, Sigma-Aldrich Co; USA) was added to each well, and the plate was placed on a shaker for 10 min to dissolve formazan crystals completely. The solutions in the wells were transferred to a 96-well plate, and the absorbance was measured using a microplate reader at 630 nm. The viability assay was run with three replications for each specimen and the negative control. The viability is presented as a percentage of the negative control, where 100% or higher corresponds to no cytotoxicity (all cells at least as viable as in the negative control), and 0% corresponds to maximal cytotoxicity (all cells dead). The optical density corresponding to cell adsorption (OD) was read for wells containing the specimens and compared to the control wells without the specimens, as in Eq. (1), to reveal the cell viability in%.

$$\text{Cell Viability}\% = \frac{OD(specimen) - OD(blank)}{OD(control) - OD(blank)} \times 100 \qquad (1)$$

In this equation, OD(specimen) corresponds to the cell adsorption of the metallic specimen, OD(blank) corresponds to the DMSO solution (background), and OD(control) corresponds to the cell adsorption rate of the cell-seeded and plasma-pre-treated well without metallic specimens.

2.9. Statistical analysis

When comparing two sets of data from independent specimens for different conditions, a student's *t*-test with unequal variance for unpaired data was used (KaleidaGraph v. 4.0). *P* values <0.05 (less than 5% probability that the two data sets are equal) are counted as statistically significant differences.

3. Results and discussion

3.1. Microstructure and surface roughness

Fig. 1 (a-c) depicts the surface morphology of the fabricated specimens after the electro-etching treatment to obtain metallographic information. A heterogeneous microstructure with tracked and scaled segments is revealed for specimens prepared from transverse (XY-plane) and longitudinal (XZ-plane) directions, respectively [34]. A network of overlapping melt pools was observed in the XY plane. In contrast, half-cylinder melt pools were observed for the XZ plane, agreeing with literature findings for powder bed fusion processes and fusion welding procedures [35]. Because of loose/solid powder around the melt pool, competitive growth occurs for LPBF, yielding various growth directions. The observed ripple solidification could be due to the sequential solidification of teardrop melt pools during the LPBF process. Vertical columnar grains in the XZ plane could be caused by heterogeneous
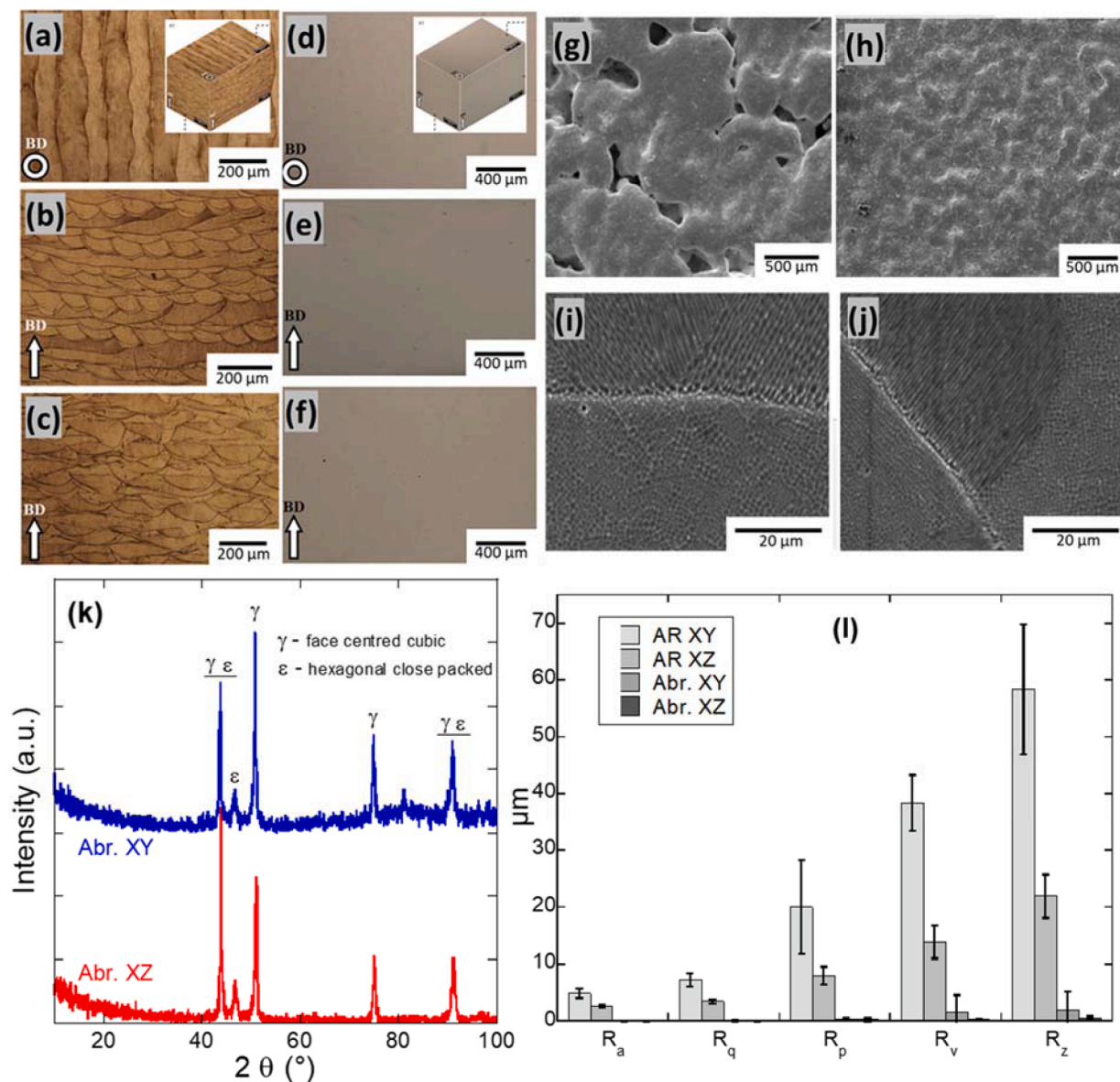
Fig. 1. Optical micrographs of different planes of the CoCrMo specimens: (a,d) top (XY plane), (b,e) mid (XZ plane), (c,f) bottom (XZ plane) areas (inset: merged sides in 3D). SEM micrographs of the printed CoCrMo specimens at (g) low magnification view of as-received XY, (h) low magnification view of as-received XZ, (i) high magnification view of the abraded and etched XY, (j) low magnification view of abraded and etched XZ. (k) XRD patterns of the abraded XY and XZ specimens. (l) Surface texture parameters of the printed CoCrMo in the as-received and abraded conditions. The error bars show the standard deviation of triplicate measurements. R_a (arithmetical mean deviation of the assessed profile), R_p (maximum peak height), R_q (root mean square average of the profile), R_v (maximum valley depth) and R_z (maximum height of the profile).

nucleation, as previous layers act as nucleation sites for subsequent layers [35].

As the formation of defects and porosity is detrimental to the functional performance of the LPBF materials, optical images were also recorded without etching and presented in Fig. 1 (d-f). ImageJ software recorded 2% and 3% porosity values for the XZ and XY planes. As-received XY and XZ specimens show distinctly different surface morphologies and roughness, as depicted in Fig. 1 (g-h), with a rougher appearance for XY. Fine columnar and cellular microstructures are visible on the surfaces of abraded/etched specimens (Fig. 1, i-j).

Different void types were observed for the abraded XY and XZ planes using optical microscopy, Fig. S1 (supplementary information). For the XY plane, only gas porosities (round) were observed; however, both gas porosities and lack of fusion defects were observed for the XZ plane. The morphology of the voids can be influenced by various factors, including energy density, heat flow and solidification of the melt pool during the LPBF process [36]. Lack of fusion defects are formed due to inadequate penetration of the molten pool of a layer into the previously printed layers. Hence, they are only seen for the XZ plane with a high density of melt pool boundaries (Fig. 1b).

XRD spectra of abraded XY and XZ specimens are presented in Fig. 1 (k), showing face-centered cubic (FCC) γ phase as the main phase in the printed specimens, while hexagonal close-packed (HCP) ε phase peaks could also be found [17,34,35]. No other phase was identified (instrumental detection limit ~5 vol.%). The ε phase derives from martensitic transformation (γ→ε) during subsequent heating processes (subsequent layers) [16,37]. Furthermore, heat treatment can alter the phase composition of CoCrMo alloy. Specifically, the heat treatment of the specimens at 750 °C for 1 h increased the transformation to martensite [38].

Fig. 1(l) depicts the surface roughness values of the abraded and as-received XY and XZ surfaces, with a higher surface roughness (R_a = 5.3

$\pm$ 0.6 μm) for the as-received XY compared to the as-received XZ (2.6 $\pm$ 0.3 μm). A similar trend was seen for the maximum profile peak height (R_z), being 20% higher for XY compared to XZ (59 $\pm$ 3.5 compared with 47 $\pm$ 2.7 μm). For abraded specimens, there was no significant difference. The higher surface roughness of the as-received XY than XZ was also confirmed by confocal microscopy, Fig. S2. For a geometrical area of 2.25 cm^2, confocal microscopy found an actual surface area of 2.79 and 2.39 cm^2 for as-received XY and XZ, respectively. The higher roughness of as-received XY (top plane, a single layer of melted and solidified powders) could be attributed to defects of material filling or the localized lack of fusion. It has been claimed that the spatter ejection of molten material from the pool could facilitate the formation of cavities and a coarser surface [20].

In all, the microstructural investigation confirms a dense LPBF printing and distinct microstructures for XY and XZ planes. As-received XY was coarser than XZ.

3.2. Surface characterization

XPS was used to determine the surface (7–10 nm) composition and the speciation of Co, Cr, and Mo, Fig. 2. Carbon, oxygen, and silicon were the three most abundant elements on the surface. Carbon originates mainly from adventitious carbon, which is well-known [39]. The C 1s high-resolution spectrum further confirms the absence of carbides and the dominance of C-C and C—H bonds, Figs. S3–S6. The high-resolution peak of O 1s revealed the dominance of a peak at 532.4 $\pm$ 0.1 eV, which can be assigned to oxygen originating from organic substances or SiO$_2$. Because of the concomitant presence of silicon, we also analyzed the Si 2p high-resolution for two of the specimens (as-received and abraded XY). Based on the peak positions (Si 2p$_{3/2}$ 102.15–102.18 eV), Fig. S7, the most probable origin is silicone [28], a common contaminant. Within the detection depth (7–10 nm), metallic peaks of Co, Cr, and Mo were detected in all cases (Figs. 2b and S3–S6), suggesting a rather thin (a few nanometers) surface oxide. Co, Cr, and Mo oxide species were relatively similar for all specimens: Co(OH)$_2$, Cr$_2$O$_3$, Cr(OH)$_3$, and Mo oxide in the valence states of IV, V, and VI. There appears to have been a consistent growth of oxidized molybdenum after the polishing procedure, which is expected for neutral water exposure [40].

3.3. Corrosion

3.3.1. Open circuit potential and cyclic polarization

The OCP shifted towards more positive potentials for all specimens and solutions during 2800 s of immersion. There was no statistically significant difference between the different surface conditions (abraded, as-received, XY, XZ) within one solution. There were significant ($P<0.05$) differences between the three solutions in all cases, except for abraded XY in CA compared with PBS-CA. PBS solution (pH 7.4) resulted in the most negative OCP (-0.27 $\pm$ 0.04 V$_{Ag/AgCl}$) after 2800 s of immersion, with PBS+CA (pH 7.4) showing a more positive OCP (-0.052 ± 0.012 V), and the most acidic solution having the most positive OCP (0.17 $\pm$ 0.038 V). This positive shift with time indicates a passivating behavior (gradual improvement of the passive film on the surface) [34] upon immersion in a physiologically relevant solution. This has been reported previously for biomedical CoCrMo alloys [41, 42].

Similar to the OCP, the E$_{corr}$ value (the corrosion potential, which is the potential at which the net current is zero during the polarization) was not significantly different among the different specimens but showed a significant difference between CA (pH 2.4) and PBS (pH 7.4), as well as between CA and PBS+CA (pH 7.4), due to the pH difference (potentials in aqueous systems shift with pH), Table 4 and Fig. 3. In PBS (Fig. 3b, Table 4), however, the E$_{corr}$ seemed to be different among the specimens (Abr. XY < Abr. XZ < AR XZ < AR XY), with a difference of at most 460 mV but this was not statistically significant ($P > 0.05$). The corrosion current density (i$_{corr}$), which is the current density determined from the intersection of the anodic and cathodic branch (linear extrapolation), was not different among the solutions and not different between the specimens in CA (pH 2.4) and PBS+CA (pH 7.4). However, in PBS (pH 7.4), there was a statistically significant ($P<0.05$) difference in corrosion current density between as-received XY (0.075$\pm$0.008 μA/cm^2) and as-received XZ (0.015$\pm$0.003 μA/cm^2), as well as between as-received XY and abraded XY (0.017$\pm$0.012 μA/cm^2). This difference cannot be explained by the difference in actual surface area (at most 25% difference, Section 3.1). Likewise, for the passive current density (here defined as the current density where the anodic branch becomes horizontal [43]), only the difference between as-received XY (0.74 $\pm$0.37 μA/cm^2) and as-received XZ (0.07$\pm$0.04 μA/cm^2) in PBS (pH 7.4) was statistically significant. Hence, there seems to be a larger influence of the plane (XY vs. XZ) for as-received surfaces, and abrasion seems to result in lower corrosion currents and a larger passive region, Fig. 3 and Table 4. This finding agrees with previous work on the corrosion of LPBF
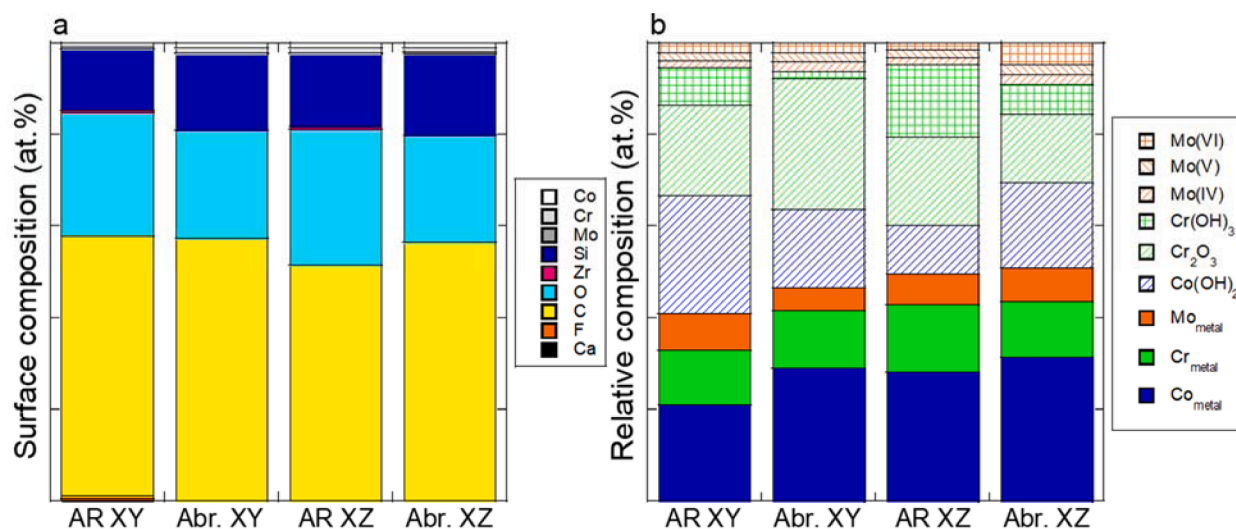

Fig. 2. Surface composition estimated from the XPS wide spectra (a) and relative surface composition and speciation of the elements Co, Cr, and Mo (b) of as-received (AR) and abraded (Abr.) CoCrMo surfaces in XY and XZ planes. Corresponding spectra are shown in Figs. S3–S7 (supplementary information).

Table. 4

Cathodic and anodic Tafel constants (βa and βc), corrosion current densities (i_{corr}), passive current densities (i_{pass}) and corrosion potentials (E_{corr}) based on potentiodynamic polarization of the LPBF CoCrMo specimens after 1 h immersion in citric acid (CA) (pH=2.4), PBS (pH 7.4), and CA + PBS (pH = 7. 4) solutions at room temperature.

Systems	Materials	Tafel parameters				
		β_a (mV)	β_c (mV)	i_{corr} (μA/cm²)	i_{pass} (μA/cm²)	E_{corr} (mV$_{Ag/AgCl}$)
CA	As-received XY	95 ± 74	169 ± 16	0.3 ± 0.2	0.8 ± 0.4	135 ± 30
	Abraded XY	22 ± 20	230 ± 139	0.004 ± 0.002	0.02 ± 0.01	−19 ± 40
	As-received XZ	290 ± 201	190 ± 96	0.1 ± 0.02	0.2 ± 0.04	140 ± 31
	Abraded XZ	37 ± 7	151 ± 19	0.001 ± 0.0004	0.02 ± 0.01	59 ± 37
PBS	As-received XY	96 ± 4	137 ± 38	0.07 ± 0.01	0.7 ± 0.4	23 ± 49
	Abraded XY	71 ± 9	171 ± 17	0.02 ± 0.01	0.3 ± 0.4	−432 ± 197
	As-received XZ	61 ± 7	191 ± 46	0.02 ± 0.003	0.07 ± 0.04	−219 ± 17
	Abraded XZ	64 ± 19	180 ± 3	0.01 ± 0.003	0.1 ± 0.1	−411 ± 117
CA+PBS	As-received XY	100 ± 1	136 ± 1	0.05 ± 0.05	0.4 ± 0.4	−84 ± ± 33
	Abraded XY	71 ± 32	57 ± 22	0.002 ± 0.002	0.01 ± 0.01	−138 ± 46
	As-received XZ	61 ± 40	91 ± 21	0.04 ± 0.05	0.2 ± 0.2	−89 ± 112
	Abraded XZ	49 ± 17	109 ± 59	0.004 ± 0.005	0.03 ± 0.04	−216 ± 114

316L [4].

There were no indications of localized corrosion (lower potential during reverse scan than during forward scan, Fig. 3), which agrees with previous work [44]. The rapid increase in current density at high potentials can hence be attributed to water oxidation and maybe transpassive dissolution but not localized corrosion [45–47]. This conclusion was further confirmed by inspection by optical microscopy after the polarization.

While there was no significant difference among solutions for the corrosion and passive corrosion density, the transpassive region (current increase at high potentials) occurred clearly at lower potentials in

PBS+CA compared to PBS (both at pH 7.4). This is supported by the work conducted on LPBF 316L in PBS and PBS + citric acid [29] and may be attributed to the formation of metal-citrate species, which can increase dissolution in some cases [4,40]. Also, there was a clear oxidation shoulder peak around 0.7 V in both solutions, which is assumed to be the formation of a phosphate-chromium complex [32].

For other alloys, porosity has been discussed as an important factor for the pitting corrosion susceptibility or repassivation ability [21]. In this study, the specimens were fabricated with the highest possible density (low porosity) and exhibited a very high pitting corrosion resistance under all conditions. As observed in this study and previous studies [48], small pores do not detrimentally affect the pitting resistance of CoCrMo alloys.

In all, the CoCrMo specimens were passive and not undergoing localized corrosion. There was an effect of the building direction for as-received specimens (highest corrosion for as-received XY) and an effect of the solution (highest currents in PBS+CA) at high potentials.

3.3.2. Electrochemical impedance spectroscopy

Fig. 4 shows Nyquist (a-c) and Bode plots (d-e) based on EIS after 1 h immersion at OCP. The Nyquist plots are all semicircular arcs indicating a typical passive state with high impedance values with capacitive behavior. The semicircle diameter in these curves equals the charge transfer resistance, which is related to corrosion resistance. The Bode plots show three distinctive regions. The absolute impedance is independent of frequency in the high frequencies (the phase angle is around 0°). In these frequencies, the impedance corresponds to the resistance of the electrolyte between working and reference electrodes. A purely capacitive response is obtained in the low to medium frequency levels. In these frequencies, the absolute impedance exhibits a linear relationship with the frequency (a slope approaching -1). In the low-frequency range, the absolute impedance is independent of the frequency.

The electrolyte resistance was higher in CA (pH 2.4) than in the PBS-containing electrolytes, Fig. 4 and Table 5. In the medium and low-frequency segments, the Bode plots represent the charge transport characteristics across the double layer and the passive oxide film, respectively. Here, the maximum phase angle values are between 70 and 90° within a wide range of frequencies (0.1 to 100 Hz). Higher values mean more stable passive oxide films and a higher corrosion resistance [49].

The simplified Randles equivalent electrical circuit (EEC) was used to fit the EIS results (Fig. 4), similar to other studies on the corrosion behavior of CoCrMo alloy in simulated physiological solutions [49–51]. The goodness of fitting (χ^2) values were below 10^{-3}. Table 5 shows the resulting fitting parameters. R_s denotes the solution resistance, R_p is the native oxide film resistance, CPE is the constant phase element, C_{eff} is the effective capacitance, and n is the phase constant exponent. A CPE
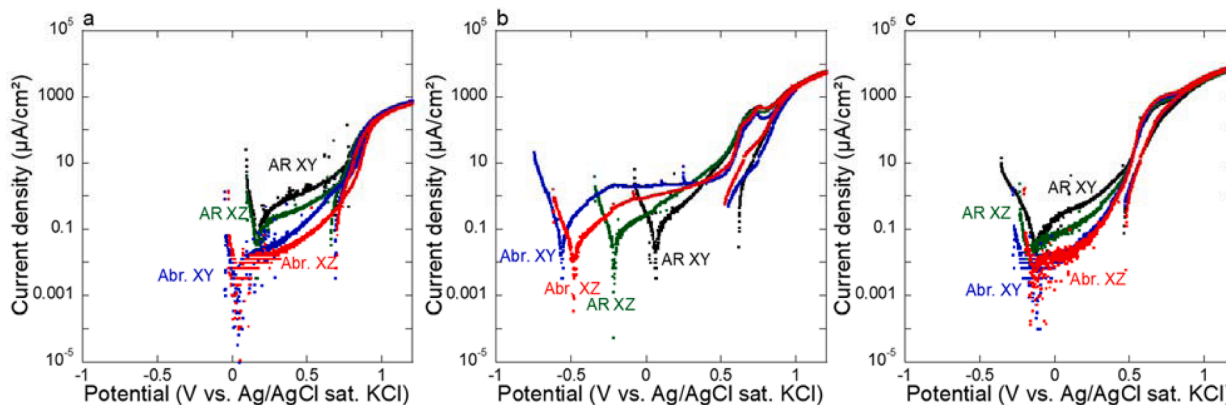

Fig. 3. Representative cyclic polarization curves (forward and reverse scans) for as-received (AR) and abraded (Abr.) CoCrMo specimens in XY and XZ plane in citric acid (pH=2.4) (a), PBS (pH 7.4) (b), and PBS + citric acid (pH = 7. 4) (c) solutions at room temperature.
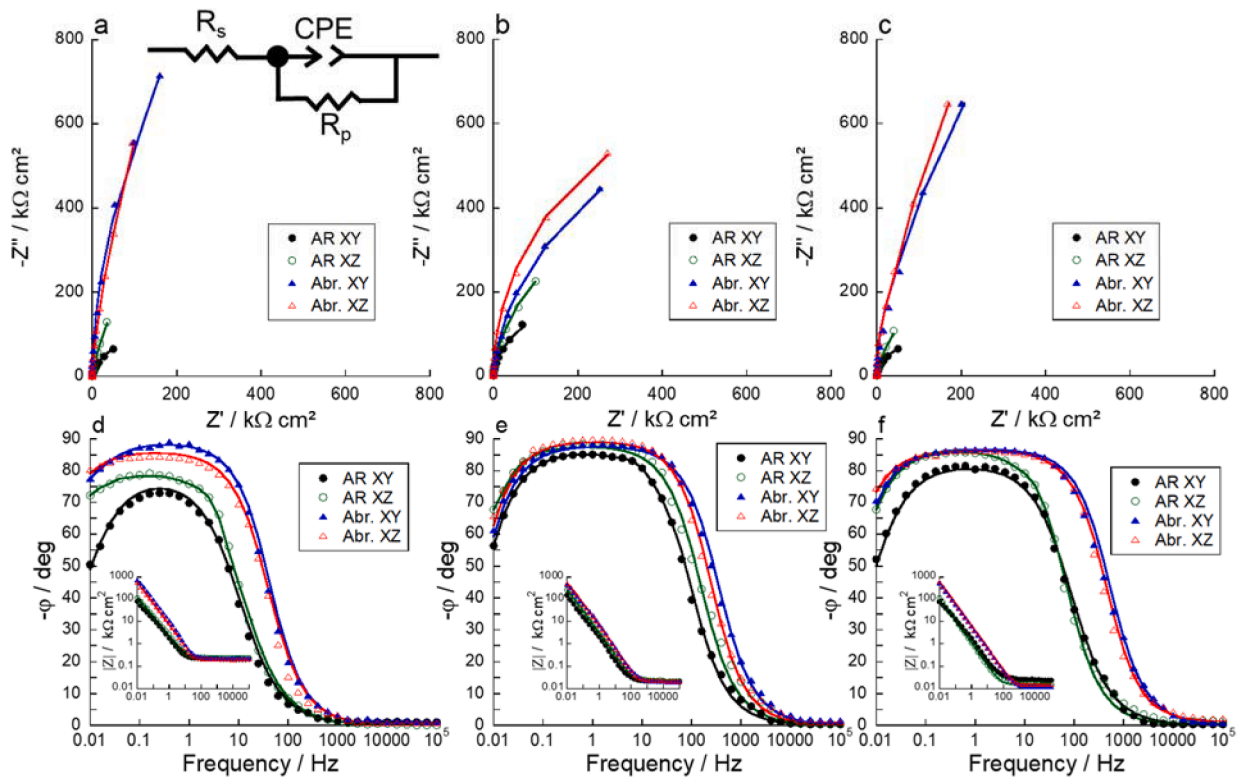
Fig. 4. Representative Nyquist (a-c), Bode phase angle (d-f), and Bode impedance (insets in d-f) plots of as-received and abraded CoCrMo in planes XY and XZ after 1 h immersion in citric acid (pH 2.4) (a, d), PBS (pH 7.4) (b, e), and PBS + citric acid (pH 7.4) (c, f) at room temperature. The inset in (a) shows the equivalent electrical circuit for the analysis of the impedance spectra (Table 5). Lines – fit; symbols – data points.

Table 5
EIS fitting parameters (average and standard deviation of two independent specimens). A one-time constant (Randles equivalent electrical circuit) was applied.

Systems	Materials	Parameters					
		R_s (Ω cm^2)	CPE (Y_0, $\mu Fcm^{-2}s^{-n}$)	C_{eff} (μFcm^{-2})	n	R_p (MΩ cm^2)	χ^2 (10^{-3})
CA	As-received XY	220 ± 0.78	123 ± 9.3	87 ± 28	0.91 ± 0.06	1.7 ± 2.2	0.52 ± 0.04
	Abraded XY	230 ± 13	19 ± 3.2	12 ± 0.53	0.93 ± 0.04	37 ± 4.6	0.36 ± 0.07
	As-received XZ	255 ± 8.8	92 ± 9.2	58 ± 11	0.89 ± 0.01	18 ± 3.0	0.58 ± 0.10
	Abraded XZ	205 ± 7.1	23 ± 2.3	15 ± 6.2	0.93 ± 0.05	39 ± 1.6	0.25 ± 0.04
PBS	As-received XY	24 ± 2.3	104 ± 20	50 ± 6.2	0.89 ± 0.01	3.9 ± 1.7	0.42 ± 0.04
	Abraded XY	23 ± 3.3	23 ± 3.9	15 ± 7.6	0.94 ± 0.04	13 ± 3.4	0.28 ± 0.04
	As-received XZ	23 ± 1.3	50 ± 1.6	18 ± 5.4	0.87 ± 0.03	7.4 ± 0.65	0.51 ± 0.13
	Abraded XZ	31 ± 2.6	27 ± 4.7	17 ± 2.5	0.94 ± 0.04	13 ± 2.8	0.48 ± 0.04
CA+PBS	As-received XY	28 ± 1.5	113 ± 6.3	74 ± 9.7	0.93 ± 0.03	1.7 ± 0.20	0.64 ± 0.04
	Abraded XY	18 ± 2.5	23 ± 3.4	15 ± 3.1	0.95 ± 0.04	25 ± 2.7	0.73 ± 0.04
	As-received XZ	17 ± 1.0	161 ± 15	97 ± 8.8	0.92 ± 0.03	3.2 ± 0.43	0.19 ± 0.04
	Abraded XZ	19 ± 0.56	20 ± 0.6	15 ± 3.2	0.97 ± 0.02	20 ± 0.61	0.21 ± 0.02

was used due to the non-ideal capacitance of the capacitive elements because of different physical phenomena, such as surface heterogeneity originating from surface roughness, pores, impurities and grain boundaries [52,53]. The impedance of the CPE is defined as $Z_{CPE}=[Y_o(jw^n)]^{-1}$] where, Y_0 is the frequency-independent constant, j is the imaginary unit ($j^2=-1$), ω is the angular frequency, and n ($0 \leq n \leq 1$) is the phase constant exponent representing surface irregularities. Depending on n, CPE can be related to a pure resistor ($n = 0$, $Y_o=R$), a pure capacitor ($n = 1$, $Y_o=C$), or the Warburg impedance ($n = 0.5$, $Y_o=W$). The C_{eff} values were determined as follows [54]:

$$C_{eff} = Q^{1/n} \times R_p^{(1-n)/n} \tag{2}$$

The effective capacitance can be linked to the film thickness as follows [55]:

$$C_{eff} = \varepsilon \times \varepsilon_0 \times \frac{A}{d} \tag{3}$$

where ε is the relative dielectric constant (ε_0 is the permittivity in vacuum), A is the surface area, and d denotes the film thickness.

The EIS data revealed that the solution, the roughness (as-received versus abraded), and the build direction influenced the barrier characteristics of the passive layers formed on the surfaces. According to the fitted data presented in Table 5, R_p was significantly ($P<0.05$) lower in PBS compared with CA and CA+PBS (only for XY) for the abraded specimens and lower in CA+PBS compared with CA for the abraded XZ specimen. This behavior can be attributed to the adsorption of citrate ions on the oxide layer and their complexation with metal ions in the oxide, which accelerates passivation (chromium enrichment due to preferential dissolution of cobalt) [32,56]. The superior passivity characteristics of the samples in this work agree with the results reported for LPBF 316L stainless steel in a citrate buffer and PBS solutions [29].

The C_{eff} was higher for the as-received compared with the abraded specimens for both XY and XZ planes, statistically significant in both PBS

(for both XY and XZ) and CA+PBS (for XZ). A similar trend was seen for CPE (statistically significant in CA and CA+PBS). Further, the C_{eff} was higher ($P<0.05$) for as-received XZ samples in CA+PBS than in PBS. Based on Eq. (3), an increase in the C_{eff} means a decrease in the thickness of the passive layer or the dielectric constant of the passive layer [57]. Hence, it seems that the passive film formation was accelerated for abraded CoCrMo surfaces and, in some cases (as-received XZ), in the presence of citrate species. A similar trend was found for R_p for as-received XZ in the solutions containing CA (higher R_p for abraded than as-received surfaces).

Hence, the barrier characteristics of the passive layer formed on the as-received surfaces (for both XY and XZ samples) were inferior to the abraded samples, and the difference in the actual surface area cannot explain this. An inferior barrier could be attributed to the higher porosity and surface defects, such as lack of fusion and non-melted metal powders, or other factors, such as the sandblasting procedure [21,58].

In line with the cyclic polarization data, the corrosion resistance, estimated from EIS, was lowest for the as-received XY. It was also lower for as-received than for abraded specimens, Fig. 4 and Table 5.

3.4. Bioactivity and biocompatibility

Any precipitation of hydroxyapatite layers on the surface of the specimens was investigated in a bioactivity assay after incubation at 37 °C (static conditions) in SBF for 7, 14, and 28 days. The specimens were evaluated using SEM (Fig. 5), and the atomic Ca/P ratio was investigated using EDS (Fig. 6). EDS further confirmed that Ca and P were the only elements of that surface layer. Fig. 5 reveals gradually increasing/covering layers of precipitates on all specimens ($P < 0.05$). After 28 days, almost the entire surface was covered with a thick layer of aggregates. The atomic Ca/P gradually increased with exposure time for all specimens, and there was no significant difference found among the specimens. After 28 days, the Ca/P ratio was 1.65±0.1, which is close to the ratio of natural hydroxyapatite of 1.67 [59].

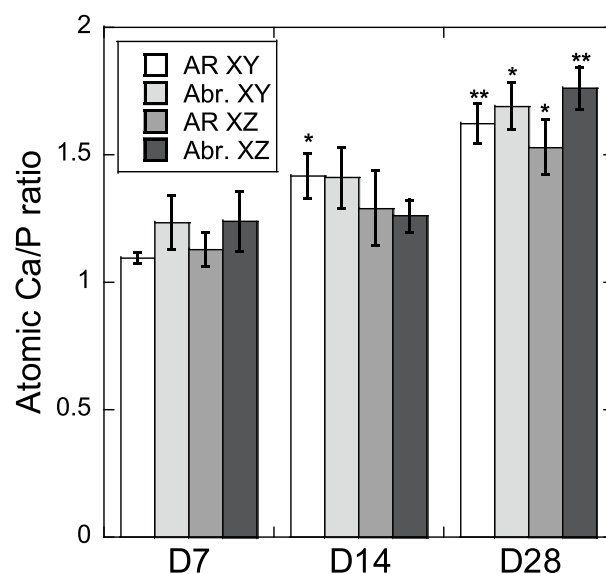Fig. 7 shows SEM images of the adhesion and expansion capability of

Fig. 6. Atomic Ca/P ratio (using EDS) of different specimens after immersion for 7 (D7), 14 (D14), and 28 (D28) days at 37 °C in simulated body fluid. The error bars show the standard deviation among triplicate measurements. The asterisks indicate statistically significant increases compared to the specimens after 7 days (D7): * - $p < 0.05$; ** - $p < 0.01$. Examples of corresponding SEM images are shown in Fig. S8.

MG63 cells cultured on the surface of as-received and abraded XY and XZ CoCrMo surfaces. Fewer cells were adhered on as-received than on polished surfaces after one day, independent of building direction. Over time, on Day 7, the rate of adhesion and cell proliferation increased sharply for all specimens. However, slightly more cells adhered to the as-received specimens after 7 days, possibly related to higher surface roughness [60]. The morphology of all cells on the surface of the
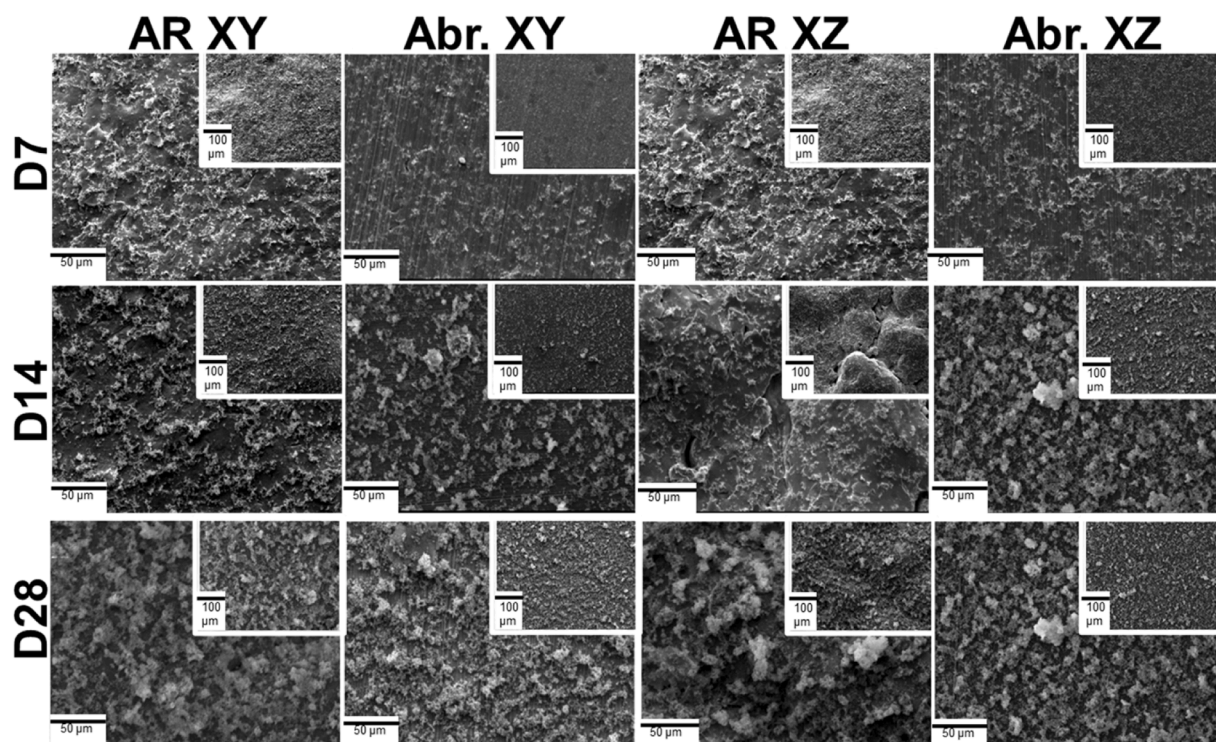

Fig. 5. SEM images of different specimens after immersion for 7 (D7), 14 (D14), and 28 (D28) days at 37 °C in simulated body fluid. Insets show overview images at lower magnification.
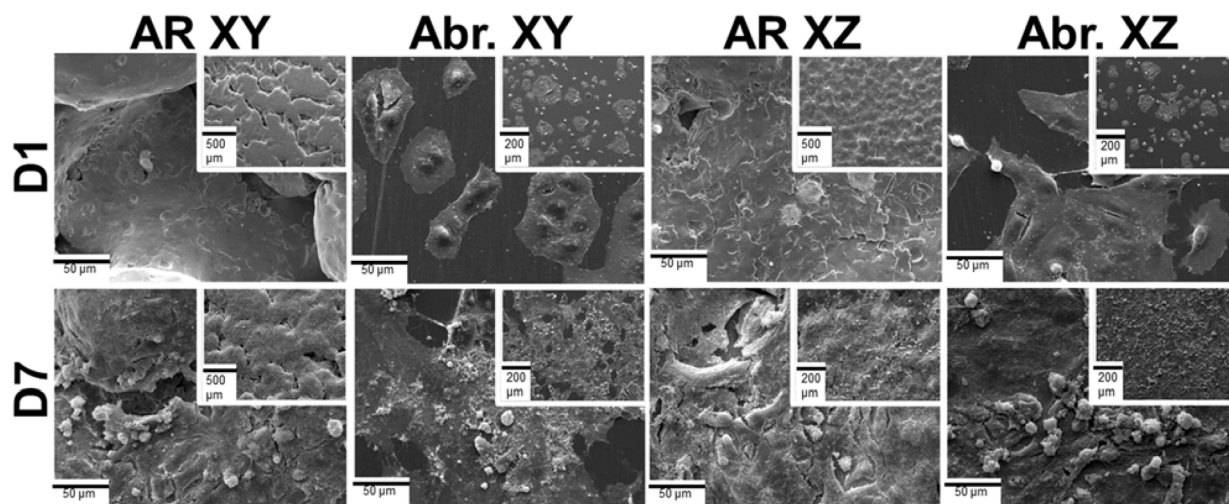
Fig. 7. SEM images of the cell-seeded as-received (AR) or abraded (Abr.) XY and XZ CoCrMo surfaces after days 1 and 7. The inset images show images at lower magnification.

specimens is relatively stretched, and the cells completely cover the surface after 7 days. Lamellipodia and filopodia can be seen at higher magnification, indicating the tendency of the cells to attach to the surface of the specimens.

The cell viability was determined using the MTT assay after one, three, and seven days, Fig. 8. There was no significant difference among the specimens. All specimens showed fully viable cells (compared to control) after one day but significantly decreased viability of cells after three and seven days. Some decrease of viability from Day 1 to 3 for the CoCrMo specimens was expected due to the control sample having better cell adhesion conditions due to the plasma treatment of the cell culture plates, which makes the well surfaces charged and hydrophilic. Thus, cells on the control surface started their proliferation phase faster than on the metallic surfaces, leading to higher viability for Day 1. The cell viability increased slightly for all specimens from Day 3 to Day 7 because, during this period, cells on the metallic specimens had enough time to secrete extracellular matrix proteins on the surface, aiding in adherence, migration, and proliferation of cells on the surface. After

three and seven days, there was a slightly higher viability, however not statistically significant ($P > 0.05$), for the as-received CoCrMo surfaces compared to their abraded counterparts. Based on the rate of cell viability in the MTT test, all specimens would be considered biocompatible materials by ISO-10993 [61].

3.5. Further discussion

As-received, rougher surfaces showed inferior corrosion barrier properties compared with abraded surfaces in this study. The difference in actual surface area cannot explain the difference. Like in this study, a negative influence of surface roughness on corrosion was reported for various LPBF materials [62–64]. It is well known that the LPBF specimens are associated with higher roughness (range from 10 μm to 30 μm) than parts fabricated with conventional methods, such as milling (~1 μm) [11]. The surface roughness of the LPBF products can be affected by factors such as the fabrication strategy, laser power, powder geometry, and heat input [65]. However, the roughness is not the only factor changing between as-received and abraded surfaces. The crystal structure, microstructure, residual stresses, unfused particles, and impacts from surface treatments (sandblasting, grinding) are also changing [16,66], so it is not straightforward to determine which physicochemical factor influenced corrosion and biocompatibility most.

While the rougher, as-received surfaces had detrimental corrosion behavior in this study, they showed higher bioactivity (adsorption of hydroxyapatite) and slightly higher cell viability. It has been reported that hydroxyapatite acts as a barrier layer and is beneficial for the corrosion resistance of CoCrMo [67]. Various factors such as porosity, surface properties, mechanical properties and ion release rate can affect the biological activities of cells [9]. Increasing surface roughness at the micro and nano scales has been shown to increase cell interaction and adhesion to the surface [2]. Therefore, the slightly increased cell viability of the rougher, as-received, CoCrMo surfaces in this study was expected.

Using potentiodynamic polarization, only the combination of citrate species and oxidative potentials resulted in higher corrosion/dissolution for CoCrMo in this study. This observation agrees with the reported corrosion current densities of CoCrMo as a function of citrate concentration [56], only slightly changing at the concentration of citrate used in this study (26 mM). The increased current of CoCrMo specimens at high oxidation potential and in the presence of citrate species is interesting from several perspectives. First, complexation caused by citrate is very similar to what is expected in physiological environments, where many biomolecules have complexing properties to metals. Citrate
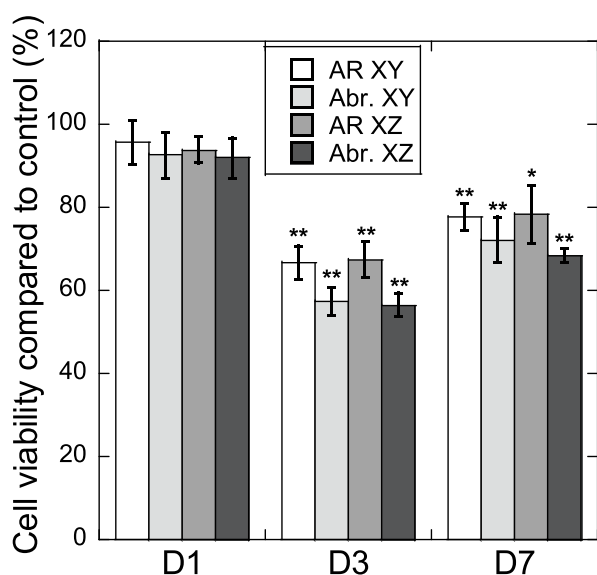

Fig. 8. Cell viability as compared to control, determined using the MTT assay after 1 (D1), 3 (D3), and 7 (D7) days at 37 °C for triplicate specimens. The asterisks indicate a statistically significant decrease (* - $P < 0.05$; ** - $P < 0.01$) in cell viability.

species are only able to complex metals at pH values, for which they are not fully protonated, so the control solution of citric acid at pH 2.4 is not a complexing solution [23]. It has previously been reported that there can be synergistic effects of oxidizing and complexing agents for the dissolution of metals from passive surface oxides, as reported for proteins and hydrogen peroxide for titanium-aluminum alloys [68]. While applied potentials are not directly relevant to the human body, they simulate inflammatory and infectious conditions under which strong oxidative redox potentials can occur [8,69]. Without any applied potential, the presence of citrate instead resulted in an increased corrosion resistance, as evident from this study's EIS measurements at open circuit potential. This agrees with findings in a combined electrochemical and XPS study on CoCrMo, suggesting that Co preferentially dissolves in the presence of citrate and that passivity is only affected at elevated potential ranges (under oxidation) in similar testing conditions as in this study [32].

This study found a higher corrosion susceptibility for as-received surfaces built in the XY plane compared with the XZ plane for highly dense LPBF CoCrMo specimens. This difference disappeared after surface abrasion – removing the influence of surface roughness and surface treatments. XPS further revealed minor differences in oxide thickness and composition. Hence, we suspect that the as-built surface, but not underlying layers or anisotropy of the microstructure, cause the differences in corrosion behavior. The XZ plane had more defects and more melt pool boundaries. Our specimens were prepared after a biomedical manufacturing protocol, using heat treatment and low-carbon CoCrMo feed powder, resulting in negligible carbide precipitates at grain boundaries. This means that any detrimental microstructure anisotropy was minimized in this study. The beneficial effects of heat treatment and low carbon have been reported previously [56]. An electrochemical study [8] on abraded LPBF CoCrMo (low carbon, but not heat treated) in NaCl with H_2O_2 revealed a higher corrosion susceptibility (lower corrosion resistance) for the XY than the XZ plane, explained by more grain boundaries and secondary precipitates. Discussions in these and other [29,49] studies have suggested that the number of grain boundaries can have both positive and negative effects on the corrosion resistance and that secondary phases and grain boundary precipitates are to be avoided. This work highlights that a suitable heat treatment strategy can eliminate any anisotropic effects of microstructure in LPBF CoCrMo.

This study is limited by its experimental conditions and design. Lower corrosion resistance under static corrosion testing conditions for the as-received XY plane was found but also higher cell viability and bioactivity for the as-received surfaces. It remains to be investigated which effects would dominate the corrosion process under long-term *in-vivo* conditions. Future studies should also examine the tribocorrosion behavior, which would be most relevant for CoCrMo alloys.

4. Conclusions

This study aimed to investigate the corrosion resistance, bioactivity, biocompatibility, and microstructure of LPBF CoCrMo (low carbon content, heat treated) in the XY and XZ plane of the building direction for as-printed (as-received) and abraded surfaces. The following main conclusions were drawn:

1 LPBF printing resulted in distinct microstructures for XY and XZ planes. As-received XY was coarser than XZ.
2 As-received XY showed the lowest corrosion resistance among the specimens. As-received surface conditions resulted in lower corrosion resistance than abraded surfaces, even when considering the actual surface area. There was no influence of building direction on corrosion resistance, bioactivity, or cell viability for abraded surfaces. Hence, the lower corrosion resistance for as-received surfaces was caused by surface factors and not microstructural features.

3 Hydroxyapatite precipitated and formed on all surfaces but slightly more on as-received (rough) surfaces. Likewise, in terms of cell viability, all surfaces counted as biocompatible. However, the as-received surfaces had slightly higher cell viability.
4 All CoCrMo surfaces exhibited passive conditions and were not showing signs of localized corrosion in citric acid (pH 2.4), PBS (pH 7.4), and PBS and citric acid (pH 7.4).
5 PBS containing the complexing citrate species from citric acid at pH 7.4 resulted in lower corrosion resistance as compared to both PBS (pH 7.4) and citric acid (pH 2.4) alone, but only at elevated (oxidative) potentials. The lowest corrosion resistance was found in PBS by electrochemical impedance spectroscopy at open circuit potential, probably due to an acceleration of passive film formation by the citrate species.

CRediT authorship contribution statement

Masoud Atapour: Conceptualization, Methodology, Validation, Formal analysis, Writing – original draft, Visualization, Supervision, Project administration, Funding acquisition. **Saber Sanaei:** Investigation, Writing – original draft. **Zheng Wei:** Investigation, Validation, Formal analysis, Writing – review & editing, Visualization. **Mohammadali Sheikholeslam:** Methodology, Investigation, Resources, Writing – original draft. **Jeffrey D. Henderson:** Investigation, Formal analysis, Writing – review & editing, Visualization. **Ubong Eduok:** Validation, Formal analysis, Writing – review & editing, Visualization. **Yara K. Hosein:** Conceptualization, Methodology, Resources, Writing – review & editing, Project administration, Funding acquisition. **David W. Holdsworth:** Resources, Writing – review & editing, Funding acquisition. **Yolanda S. Hedberg:** Conceptualization, Methodology, Validation, Formal analysis, Resources, Writing – review & editing, Visualization, Supervision, Project administration, Funding acquisition. **Hamid Reza Ghorbani:** Methodology, Resources, Writing – review & editing, Supervision, Funding acquisition.

Declaration of Competing Interest

The authors declare the following financial interests/personal relationships which may be considered as potential competing interests: Yolanda Hedberg and David Holdsworth report financial support was provided by Natural Sciences and Engineering Research Council of Canada. Yolanda Hedberg reports financial support was provided by Canada Research Chairs. Yolanda Hedberg reports financial support was provided by Taiho Kogyo Tribology Research Foundation. Yolanda Hedberg reports financial support was provided by Wolfe-Western Fellowship. Hamid Reza Ghorbani reports financial support was provided by Avicenna Center of Excellence. Masoud Atapour reports financial support was provided by Isfahan Research Network.

Data availability

Data will be made available on request.

Acknowledgments

We would like to acknowledge the assistance of Engineering Technician David Pacifico and Production Manager Tom Chmiel at Additive Design In Surgical Solutions, Inc. One of the authors (Masoud Atapour) wishes to express gratitude to the Invited Collaborative Research Program (ICRP), Center for International Scientific Studies and Collaboration, Ministry of Science, Research and Technology of Iran, for their support. Also, we wish to acknowledge the support from the Avicenna Center of Excellence (ACE).

Supplementary materials

Supplementary material associated with this article can be found, in the online version, at doi:10.1016/j.electacta.2023.142059.

References

[1] A. Nouri, A.R. Shirvan, Y. Li, C. Wen, Additive manufacturing of metallic and polymeric load-bearing biomaterials using laser powder bed fusion: a review, J. Mater. Sci. Technol. 94 (2021) 196–215.

[2] D. Shekhawat, A. Singh, A. Bhardwaj, A. Patnaik, A short review on polymer, metal and ceramic based implant materials, IOP Conf. Ser. Mater. Sci. Eng. (2021), 012038.

[3] J. Zhou, Z. Zhang, J. Joseph, X. Zhang, B.E. Ferdows, D.N. Patel, W. Chen, G. Banfi, R. Molinaro, D. Cosco, Biomaterials and nanomedicine for bone regeneration: progress and future prospects, Exploration (2021), 20210011.

[4] M. Atapour, X. Wang, K. Färnlund, I. Odnevall Wallinder, Y. Hedberg, Corrosion and metal release investigations of selective laser melted 316L stainless steel in a synthetic physiological fluid containing proteins and in diluted hydrochloric acid, Electrochim. Acta 354 (2020), 136748.

[5] E.R. Ghomi, F. Khosravi, R.E. Neisiany, S. Singh, S. Ramakrishna, Future of additive manufacturing in healthcare, Curr. Opin. Biomed. Eng. 17 (2021), 100255.

[6] K. Zhou, J. Chen, T. Wang, Y. Su, L. Qiao, Y. Yan, Effect of surface energy on protein adsorption behaviours of treated CoCrMo alloy surfaces, Appl. Surf. Sci. 520 (2020), 146354.

[7] D. de Castro Girão, M. Béreš, A.L. Jardini, R.M. Filho, C.C. Silva, A. de Siervo, H. F. Gomes de Abreu, W.S. Araújo, An assessment of biomedical CoCrMo alloy fabricated by direct metal laser sintering technique for implant applications, Mater. Sci. Eng. C 107 (2020), 110305.

[8] Y. Hu, C. Dong, D. Kong, M. Ao, J. Ding, X. Ni, L. Zhang, P. Yi, X. Li, Degradation behaviour of selective laser melted CoCrMo alloys in H2O2-containing chloride solutions, Corros. Sci. 195 (2022), 109981.

[9] A. Bandyopadhyay, A. Shivaram, M. Isik, J.D. Avila, W.S. Dernell, S. Bose, Additively manufactured calcium phosphate reinforced CoCrMo alloy: bio-tribological and biocompatibility evaluation for load-bearing implants, Addit. Manuf. 28 (2019) 312–324.

[10] G. Cortis, I. Mileti, F. Nalli, E. Palermo, L. Cortese, Additive manufacturing structural redesign of hip prostheses for stress-shielding reduction and improved functionality and safety, Mech. Mater. 165 (2022), 104173.

[11] D. Kong, C. Dong, X. Ni, X. Li, Corrosion of metallic materials fabricated by selective laser melting, npj Mater. Degrad. 3 (2019) 24.

[12] R. Mirea, I.M. Biris, L.C. Ceatra, R. Ene, A. Paraschiv, A.T. Cucuruz, G. Sbarcea, E. Popescu, T. Badea, *In Vitro* physical-chemical behaviour assessment of 3D-printed CoCrMo alloy for orthopaedic implants, Metals 11 (2021) 857.

[13] Y. Hedberg, I. Odnevall Wallinder, Metal release and speciation of released chromium from a biomedical CoCrMo alloy into simulated physiologically relevant solutions, J. Biomed. Mater. Res. B 102 (2014) 693–699.

[14] G. Cornacchia, S. Cecchel, D. Battini, C. Petrogalli, A. Avanzini, Microstructural, mechanical, and tribological characterization of selective laser melted CoCrMo alloy under different heat treatment conditions and hot isostatic pressing, Adv. Eng. Mater. 24 (2022), 2100928.

[15] H. Li, H. Guo, F. Shen, D. Lou, W. Xia, X. Fang, Tribological and corrosion performance of the plasma-sprayed conformal ceramic coating on selective laser melted CoCrMo alloy, J. Mech. Behav. Biomed. Mater. 119 (2021), 104520.

[16] Y. Hedberg, B. Qian, S. Zhijian, S. Virtanen, I. Odnevall Wallinder, *In-vitro* biocompatibility of CoCrMo dental alloys fabricated by selective laser melting, Dent. Mater. 30 (2014) 525–534.

[17] J. Li, H. Ren, C. Liu, S. Shang, The effect of specific energy density on microstructure and corrosion resistance of CoCrMo alloy fabricated by laser metal deposition, Materials 12 (2019) 1321.

[18] X. Dong, Q. Sun, Y. Zhou, Y. Qu, H. Shi, B. Zhang, S. Xu, W. Liu, N. Li, J. Yan, Influence of microstructure on corrosion behavior of biomedical Co-Cr-Mo-W alloy fabricated by selective laser melting, Corros. Sci. 170 (2020), 108688.

[19] Y. Kajima, A. Takaichi, N. Kittikundecha, H.L. Htat, H.H.W. Cho, Y. Tsutsumi, T. Hanawa, N. Wakabayashi, T. Yoneyama, Reduction in anisotropic response of corrosion properties of selective laser melted Co–Cr–Mo alloys by post-heat treatment, Dent. Mater. 37 (2021) e98–e108.

[20] L. Tonelli, A. Fortunato, L. Ceschini, CoCr alloy processed by Selective Laser Melting (SLM): effect of laser energy density on microstructure, surface morphology, and hardness, J. Manuf. Process. 52 (2020) 106–119.

[21] M. Atapour, X. Wang, M. Persson, I. Odnevall Wallinder, Y.S. Hedberg, Corrosion of binder jetting additively manufactured 316L stainless steel of different surface finish, J. Electrochem. Soc. 167 (2020), 131503.

[22] N. Mazinanian, I. Odnevall Wallinder, Y. Hedberg, Influence of citric acid on the metal release of stainless steels, Corros. Sci. Technol. 14 (2015) 166–171.

[23] N. Mazinanian, Y.S. Hedberg, Metal release mechanisms for passive stainless steel in citric acid at weakly acidic pH, J. Electrochem. Soc. 163 (2016) C686–C693.

[24] Y. Hedberg, N. Mazinanian, I. Odnevall Wallinder, Metal release from stainless steel powders and massive sheet – comparison and implication for risk assessment of alloys, Env. Sci. Process. Impact. 15 (2013) 381–392.

[25] A. Kocijan, I. Milošev, B. Pihlar, The influence of complexing agent and proteins on the corrosion of stainless steels and their metal components, J. Mater. Sci. Mater. Med. 14 (2003) 69–77.

[26] M.C. Biesinger, B.P. Payne, A.P. Grosvenor, L.W.M. Lau, A.R. Gerson, R.S.C. Smart, Resolving surface chemical states in XPS analysis of first row transition metals, oxides and hydroxides: cr, Mn, Fe, Co and Ni, Appl. Surf. Sci. 257 (2011) 2717–2730.

[27] J. Baltrusaitis, B. Mendoza-Sanchez, V. Fernandez, R. Veenstra, N. Dukstiene, A. Roberts, N. Fairley, Generalized molybdenum oxide surface chemical state XPS determination via informed amorphous sample model, Appl. Surf. Sci. 326 (2015) 151–161.

[28] M.C. Biesinger, X-ray photoelectron spectroscopy (XPS) reference pages, http://www.xpsfitting.com/search/label/chromium, accessed 2023-01-22, 2023.

[29] N.S. Al-Mamun, K. Mairaj Deen, W. Haider, E. Asselin, I. Shabib, Corrosion behavior and biocompatibility of additively manufactured 316L stainless steel in a physiological environment: the effect of citrate ions, Addit. Manuf. 34 (2020), 101237.

[30] G.S. Duffó, E.Q. Castillo, Development of an artificial saliva solution for studying the corrosion behavior of dental alloys, Corrosion 60 (2004) 594–602.

[31] I. Milosev, H.-H. Strehblow, The behavior of stainless steels in physiological solution containing complexing agent studied by X-ray photoelectron spectroscopy, J. Biomed. Mater. Res. 52 (2000) 404–412.

[32] I. Milošev, H.H. Strehblow, The composition of the surface passive film formed on CoCrMo alloy in simulated physiological solution, Electrochim. Acta 48 (2003) 2767–2774.

[33] T. Kokubo, H. Takadama, How useful is SBF in predicting *in vivo* bone bioactivity? Biomaterials 27 (2006) 2907–2915.

[34] H. Li, H. Wang, D. Lou, W. Xia, X. Fang, Microstructural features of biomedical cobalt–chromium–molybdenum (CoCrMo) alloy from powder bed fusion to aging heat treatment, J. Mater. Sci. Technol. 45 (2020) 146–156.

[35] S.L. Sing, S. Huang, W.Y. Yeong, Effect of solution heat treatment on microstructure and mechanical properties of laser powder bed fusion produced cobalt-28chromium-6molybdenum, Mater. Sci. Eng. A 769 (2020), 138511.

[36] M.A. Aripin, Z. Sajuri, N.H. Jamadon, A.H. Baghdadi, J. Syarif, I.F. Mohamed, A. M. Aziz, Effects of build orientations on microstructure evolution, porosity formation, and mechanical performance of selective laser melted 17-4 PH stainless steel, Metals 12 (2022) 1968.

[37] K. Yamanaka, M. Mori, Y. Koizumi, A. Chiba, Local strain evolution due to athermal γ→ ε martensitic transformation in biomedical CoCrMo alloys, J. Mech. Behav. Biomed. Mater. 32 (2014) 52–61.

[38] Y. Zhang, W. Lin, Z. Zhai, Y. Wu, R. Yang, Z. Zhang, Enhancing the mechanical property of laser powder bed fusion CoCrMo alloy by tailoring the microstructure and phase constituent, Mater. Sci. Eng. A 862 (2023), 144449.

[39] M.C. Biesinger, Accessing the robustness of adventitious carbon for charge referencing (Correction) purposes in XPS analysis: insights from a multi-user facility data review, Appl. Surf. Sci. (2022), 153681.

[40] Z. Wei, V. Romanovski, L. Filho, C. Persson, Y.S. Hedberg, Metal release from a biomedical CoCrMo Alloy in mixed protein solutions under static and sliding conditions: effects of protein aggregation and metal precipitation, J. Bio Tribo Corros. 8 (2022) 19.

[41] M. Sovar, C. Ducu, D. Iordachescu, I. Demetrescu, Stability of bioactivated Co-Cr alloys in biological environment, Key Eng. Mater. (2008) 737–740. Trans Tech Publ.

[42] A.W.E. Hodgson, S. Kurz, S. Virtanen, V. Fervel, C.O.A. Olsson, S. Mischler, Passive and transpassive behaviour of CoCrMo in simulated biological solutions, Electrochim. Acta 49 (2004) 2167–2178.

[43] E. Mahlooji, M. Atapour, S. Labbaf, Electrophoretic deposition of Bioactive glass–Chitosan nanocomposite coatings on Ti-6Al-4V for orthopedic applications, Carbohydr. Polym. 226 (2019), 115299.

[44] E. Bettini, T. Eriksson, M. Boström, C. Leygraf, J. Pan, Influence of metal carbides on dissolution behavior of biomedical CoCrMo alloy: SEM, TEM and AFM studies, Electrochim. Acta 56 (2011) 9413–9419.

[45] R.W.W. Hsu, C.C. Yang, C.A. Huang, Y.S. Chen, Electrochemical corrosion studies on Co–Cr–Mo implant alloy in biological solutions, Mater. Chem. Phys. 93 (2005) 531–538.

[46] E. Liverani, A. Balbo, C. Monticelli, A. Leardini, C. Belvedere, A. Fortunato, Corrosion resistance and mechanical characterization of ankle prostheses fabricated via selective laser melting, Procedia CIRP 65 (2017) 25–31.

[47] C. Valero Vidal, A. Igual Muñoz, Electrochemical characterisation of biomedical alloys for surgical implants in simulated body fluids, Corros. Sci. 50 (2008) 1954–1961.

[48] G. Sander, S. Thomas, V. Cruz, M. Jurg, N. Birbilis, X. Gao, M. Brameld, C. Hutchinson, On the corrosion and metastable pitting characteristics of 316L

stainless steel produced by selective laser melting, J. Electrochem. Soc. 164 (2017) C250.

[49] X. Gong, Y. Li, Y. Nie, Z. Huang, F. Liu, L. Huang, L. Jiang, H. Mei, Corrosion behaviour of CoCrMo alloy fabricated by electron beam melting, Corros. Sci. 139 (2018) 68–75.

[50] A. Ribeiro, A. Alves, L. Rocha, F. Silva, F. Toptan, Synergism between corrosion and wear on CoCrMo– Al2O3 biocomposites in a physiological solution, Tribol. Int. 91 (2015) 198–205.

[51] D. Xiang, X. Sui, X. Tan, J. Hao, Z. Wang, Z. Liao, W. Liu, S. Tor, Improving biotribological properties and corrosion resistance of CoCrMo alloy via a Cr-GLC nanocomposite film in simulated body fluids, Surf. Coat. Technol. 378 (2019), 124840.

[52] C.V. Vidal, A.O. Juan, A.I. Muñoz, Adsorption of bovine serum albumin on CoCrMo surface: effect of temperature and protein concentration, Colloid Surf. B 80 (2010) 1–11.

[53] R. Kötz, M. Carlen, Principles and applications of electrochemical capacitors, Electrochim. Acta 45 (2000) 2483–2498.

[54] B. Hirschorn, M.E. Orazem, B. Tribollet, V. Vivier, I. Frateur, M. Musiani, Determination of effective capacitance and film thickness from constant-phase-element parameters, Electrochim. Acta 55 (2010) 6218–6227.

[55] R. Namus, W. Rainforth, The influence of cathodic potentials on the surface oxide layer status and tribocorrosion behaviour of Ti6Al4V and CoCrMo alloys in simulated body fluid, Biotribology 30 (2022), 100212.

[56] A. Kocijan, I. Milošev, D.K. Merl, B. Pihlar, Electrochemical study of Co-based alloys in simulated physiological solution, J. Appl. Electrochem. 34 (2004) 517–524.

[57] A.I. Muñoz, S. Mischler, Interactive effects of albumin and phosphate ions on the corrosion of CoCrMo implant alloy, J. Electrochem. Soc. 154 (2007) C562–C570.

[58] B. Zhang, Y. Li, Q. Bai, Defect formation mechanisms in selective laser melting: a review, Chin. J. Mech. Eng. 30 (2017) 515–527.

[59] R. Chaharmahali, A. Fattah-alhosseini, K. Babaei, Surface characterization and corrosion behavior of calcium phosphate (Ca-P) base composite layer on Mg and its alloys using plasma electrolytic oxidation (PEO): a review, J. Magnes. Alloys 9 (2021) 21–40.

[60] J.I. Rosales-Leal, M.A. Rodríguez-Valverde, G. Mazzaglia, P.J. Ramón-Torregrosa, L. Díaz-Rodríguez, O. García-Martínez, M. Vallecillo-Capilla, C. Ruiz, M. Cabrerizo-Vílchez, Effect of roughness, wettability and morphology of engineered titanium surfaces on osteoblast-like cell adhesion, Colloid Surf. A 365 (2010) 222–229.

[61] ISO, ISO 10993-1, "Biological evaluation of medical devices Part 1: evaluation and testing within a risk management process", (2018).

[62] A. Leon, E. Aghion, Effect of surface roughness on corrosion fatigue performance of AlSi10Mg alloy produced by Selective Laser Melting (SLM), Mater. Charact. 131 (2017) 188–194.

[63] L.R. Hilbert, D. Bagge-Ravn, J. Kold, L. Gram, Influence of surface roughness of stainless steel on microbial adhesion and corrosion resistance, Int. Biodeterior. Biodegrad. 52 (2003) 175–185.

[64] D.D. Deligianni, N. Katsala, S. Ladas, D. Sotiropoulou, J. Amedee, Y. Missirlis, Effect of surface roughness of the titanium alloy Ti–6Al–4V on human bone marrow cell response and on protein adsorption, Biomaterials 22 (2001) 1241–1251.

[65] F. Calignano, D. Manfredi, E. Ambrosio, L. Iuliano, P. Fino, Influence of process parameters on surface roughness of aluminum parts produced by DMLS, Int. J. Adv. Manuf. Technol. 67 (2013) 2743–2751.

[66] P. Panigrahi, Y. Liao, M.T. Mathew, A. Fischer, M.A. Wimmer, J.J. Jacobs, L. D. Marks, Intergranular pitting corrosion of CoCrMo biomedical implant alloy, J. Biomed. Mater. Res. B 102 (2014) 850–859.

[67] N.N. Khobragade, A.V. Bansod, K.V. Giradkar, A.P. Patil, K. Jagtap, R. Pawde, A. P. Moon, Effect of concentration and surface roughness on corrosion behavior of Co–Cr–Mo alloy in hyaluronic acid, Mater. Res. Express 5 (2018), 015403.

[68] Y.S. Hedberg, M. Žnidaršič, G. Herting, I. Milošev, I. Odnevall Wallinder, Mechanistic insight on the combined effect of albumin and hydrogen peroxide on surface oxide composition and extent of metal release from Ti6Al4V, J. Biomed. Mater. Res. B 107 (2019) 858–867.

[69] A. Larsen, M. Stoltenberg, G. Danscher, *In vitro* liberation of charged gold atoms: autometallographic tracing of gold ions released by macrophages grown on metallic gold surfaces, Histochem. Cell. Biol. 128 (2007) 1–6.